

Integrated analysis of plasma rotation effect on HL-3 hybrid scenario

Miao Xue(薛淼), Guo-Yao Zheng(郑国尧), Lei Xue(薛雷), Jia-Xian Li(李佳鲜), Shuo Wang(王硕), Hai-Long Du(杜海龙), Yi-Ren Zhu(朱毅仁), and Yue Zhou(周月)

Citation: Chin. Phys. B, 2024, 33 (**8**): 084703. DOI: 10.1088/1674-1056/ad43d3

What follows is a list of articles you may be interested in

Combustion of a single magnesium particle in water vapor

Huang Li-Ya (黄利亚), Xia Zhi-Xun (夏智勋), Zhang Wei-Hua (张为华), Huang Xu (黄序), Hu Jian-Xin (胡建新)
Chin. Phys. B, 2015, 24 (**9**): 094702. DOI: 10.1088/1674-1056/24/9/094702

Partial slip effect on non-aligned stagnation point nanofluid over a stretching convective surface

S. Nadeem, Rashid Mehmood, Noreen Sher Akbar
Chin. Phys. B, 2015, 24 (**1**): 014702. DOI: 10.1088/1674-1056/24/1/014702

Integrated analysis of plasma rotation effect on HL-3 hybrid scenario

Miao Xue(薛淼), Guo-Yao Zheng(郑国尧), Lei Xue(薛雷)†, Jia-Xian Li(李佳鲜), Shuo Wang(王硕), Hai-Long Du(杜海龙), Yi-Ren Zhu(朱毅仁), and Yue Zhou(周月)

Southwestern Institute of Physics, Chengdu 610000, *China*

(Received 13 December 2023; revised manuscript received 25 April 2024; accepted manuscript online 26 April 2024)

The hybrid scenario, which has good confinement and moderate MHD instabilities, is a proposed operation scenario for international thermonuclear experimental reactor (ITER). In this work, the effect of plasma rotation on the HL-3 hybrid scenario is analyzed with the integrated modeling framework OMFIT. The results show that toroidal rotation has no obvious effect on confinement with a high line averaged density of $n_{\rm bar} \sim 7 \times 10^{19}$ m^{-3}. In this case, the ion temperature only changes from 4.7 keV to 4.4 keV with the rotation decreasing from 10^5 rad/s to 10^3 rad/s, which means that the turbulent heat transport is not dominant. While in the scenarios characterized by lower densities, such as $n_{\rm bar} \sim 4 \times 10^{19}$ m^{-3}, turbulent transport becomes dominant in determining heat transport. The ion temperature rises from 3.8 keV to 6.1 keV in the core as the rotation velocity increases from 10^3 rad/s to 10^5 rad/s. Despite the ion temperature rising, the rotation velocity does not obviously affect electron temperature or density. Additionally, it is noteworthy that the variation in rotation velocity does not significantly affect the global confinement of plasma in scenarios with low density or with high density.

Keywords: HL-3, hybrid scenario, toroidal rotation, integrated modeling

PACS: 47.50.Cd, 98.62.Dm **DOI:** 10.1088/1674-1056/ad43d3

1. Introduction

International Thermonuclear Experimental Reactor (ITER) aims to demonstrate the feasibility of fusion energy production in both the physics and engineering aspects. The hybrid scenario is proposed for ITER operation,[1] which can provide long burning time and high neutron flux for engineering tests. This scenario could result in high-performance plasma and has been demonstrated to be robust.[2–5]

The hybrid scenario is characterized by a flat core safety factor (q) profile with a central q value close to 1.[6] Magnetohydrodynamic (MHD) instabilities such as sawtooth can be avoided due to this special q profile.[7] Previous researches have shown that the combination of low magnetic shear and electromagnetic stabilization can increase the energy confinement time.[8]

Moreover, rotation is also an essential factor affecting the confinement of tokamak operation,[9] even under the condition of high confinement, such as super-H mode operation.[10] However, other research results show that the rotation has a smaller effect on the confinement of tokamak high $\beta_{\rm p}$ operation.[11] While the effect of rotation on hybrid operation has not been sufficiently studied. Nowadays, the toroidal rotation angular velocity in a tokamak is usually larger than 10^5 rad/s.[12] Besides, for ITER, the simulation results show that its toroidal rotation angular velocity is at a level of 10^4 rad/s[13] due to the limited torque provided by the neutral beam injection (NBI) system, which may result in MHD instabilities and poor confinement.

The HL-3 is a new tokamak at the Southwestern Institute of Physics (SWIP), which achieved 1-MA plasma current discharge in 2022.[14] One of its main missions is to develop high-performance hybrid operation. The main parameters of HL-3 are as follows: major radius $R = 1.78$ m, minor radius $a = 0.65$ m, toroidal field $B_{\rm t}$ up to 3 T, maximum plasma current $I_{\rm p}$ up to 3 MA, elongation $\kappa \leq 1.8$, triangularity $\delta \leq 0.5$. The total power capacity of auxiliary heating and current drive (H & CD) systems exceeds 30 MW, including co-NBI (the neutral beam injection oriented toroidally in the same direction as the plasma current) and counter-NBI (the neutral beam injection oriented toroidally in the opposite direction to the plasma current), electron cyclotron waves (ECW), and lower hybrid waves (LHW).

This paper is to address the following issues by the 1.5-D integrated modeling framework OMFIT:[15] (i) analyzing the influence of toroidal rotation on the global confinement of hybrid operation quantitatively; (ii) understanding when the toroidal rotation effect must be addressed.

The rest of this paper is organized as follows. In Section 2, the iterative workflow and the setup of simulation parameters are introduced briefly. A series of hybrid scenarios with different toroidal rotations is designed and analyzed for HL-3 by using NBI+ECW in Section 3. The effect of rotation velocity on the hybrid scenario is analyzed at high densities in Section 4. Finally, some conclusions are drawn from the present study in Section 5.

†Corresponding author. E-mail: xuelei@swip.ac.cn

© 2024 Chinese Physical Society and IOP Publishing Ltd

2. Integrated analysis workflow

The OMFIT takes a time-independent method to calculate the steady state self-consistent solver for the flat top phase.[16] For core simulations, a combination of the two-dimensional (2D) equilibrium code EFIT[17] and the one-dimensional (1D) transport codes ONETWO[18] & TGYRO[19] is utilized. The pedestal region is handled by EPED.[20] Within ONETWO, the NUBEAM[21] and TORAY[22] codes are employed to calculate H & CD through NBI and ECW, respectively. The bootstrap current is calculated by the Sauter model. TGYRO employs two codes, TGLF and NEO, for transport, respectively. NEO is a neoclassical transport code, and TGLF is responsible for calculating turbulent transport. Electromagnetic effect, fast ion, and $E \times B$ shear effect in the calculation of turbulent transport are considered in TGLF. The kinetic profiles of the pedestal and core regions are smoothly connected by using cubic interpolation. The workflow of OMFIT is widely used in operation scenario design for ITER[23] and CFETR,[24,25] as shown in Fig. 1.

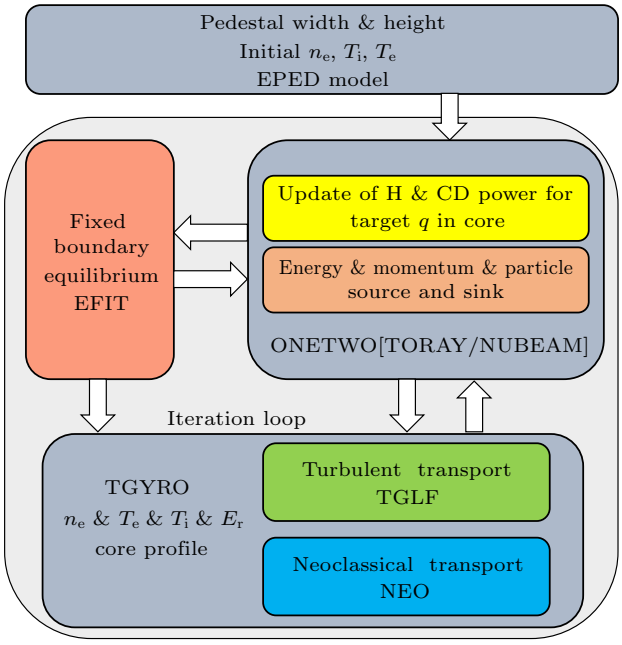


Fig. 1. Workflow for integrated modeling of HL-3 hybrid scenario.

In the simulation, a lower single-null divertor configuration is employed, with an elongation (κ) of 1.7 and a triangularity (δ) of 0.5, as depicted in Fig. 2. The off-axis electron cyclotron current drive (ECCD) is essential to obtain a flat q profile in the core, and it depends on both the toroidal magnetic field (B_t) and plasma density. The values of the plasma current (I_p) and the B_t chosen for the hybrid scenario are based on the characteristics of q_{95} and the position of the ECCD. Specifically, I_p is set to 1 MA, and B_t is maintained at 1.9 T, as listed in Table 1. The main ion is deuterium, and the impurity ion is carbon. The ion density profiles are calculated according to the quasi-neutral condition and the fixed effective charge number (Z_{eff}) of 2.0.

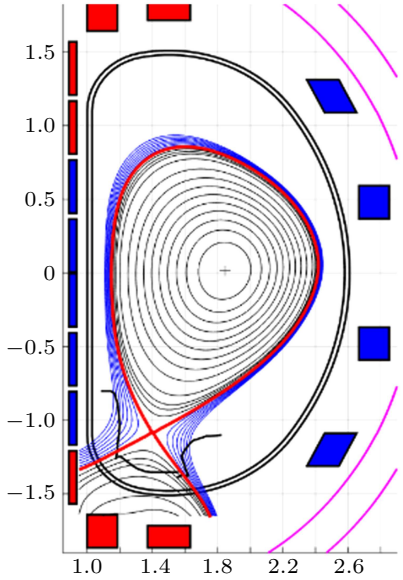


Fig. 2. HL-3 equilibrium configuration for hybrid scenario.

Table 1. Main parameters of HL-3 hybrid scenario.

Parameter	I_p (MA)	B_t (T)	R (m)	a (m)	κ	δ
Value	1	1.9	1.78	0.6	1.7	0.5

3. Hybrid scenario with low-density

In the HL-3 tokamak, we investigate the hybrid scenario characterized by a low-density plasma with a line averaged density $n_{bar} \sim 4 \times 10^{19}$ m^{-3}. This scenario utilizes 4.5 MW of NBI and 4.4 MW of ECW for auxiliary heating and current drive. Two distinct ECW systems are included in this scenario. The first ECW system, with a power value of 0.4 MW (ECW1), enhances the safety factor slightly above unity at the magnetic axis to avoid sawtooth oscillations. The second one, with 4 MW (ECW2), broadens the flat region of the q profile up to $\rho \sim 0.4$. Both of the ECW systems are launched from the midplane, with a frequency of 105 GHz. The ECW1 is launched, with poloidal and toroidal angles set to 106° and 194°, respectively. The ECW2 is launched, with poloidal and toroidal angles set to 93° and 210° as shown in Table 2. The specific trajectory and absorption locations of ECW2 are shown in Fig. 3. The co-NBI is applied to the NBI system, with a tangency major radius of 1.2 m and beam energy value of 80 keV. The parameters of NBI are listed in Table 3. The co-NBI supplies a torque of 3.63 N·m to the plasma.

Table 2. Parameters for electron cyclotron current drive and heating in HL-3.

Parameter	Power (MW)	Frequency (GHz)	Launch position	Angle
			$[R, Z]$ (cm)	[polar, toroidal] (°)
ECW1	4	105	[280, 10]	[106, 194]
ECW2	0.4	105	[280, 10]	[93, 210]

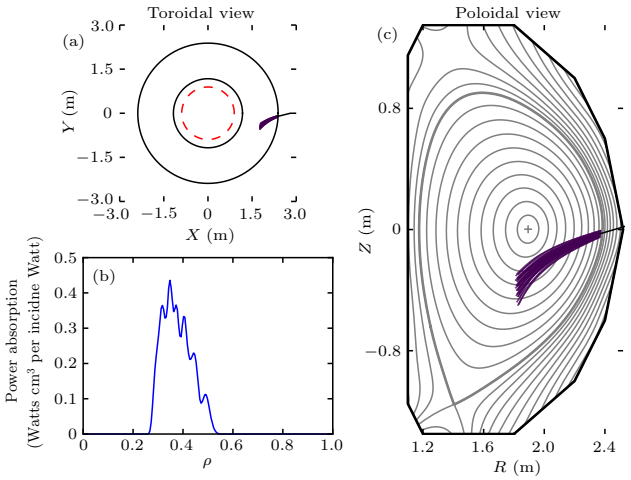


Fig. 3. (a) Traces projected on toroidal plane, (b) power deposited profile, (c) traces projected on poloidal plane of off-axis electron cyclotron heating & current drive.

Table 3. Parameters for neutral beam current drive and heating in HL-3.

Parameter	Power (MW)	Energy (keV)	Rtcena (cm)
Value	4.5	80	120

In Fig. 4, the auxiliary current drive, the bootstrap, and the ohmic current establish a flat q profile in the core, maintaining the values of q consistently in the range from 1 to 1.5. There is a weak shear near the edge of the q profile, corresponding to the high bootstrap current in Fig. 4(a). The bootstrap current accounts for 49% of the total current, while the ohmic current contributes 13%.

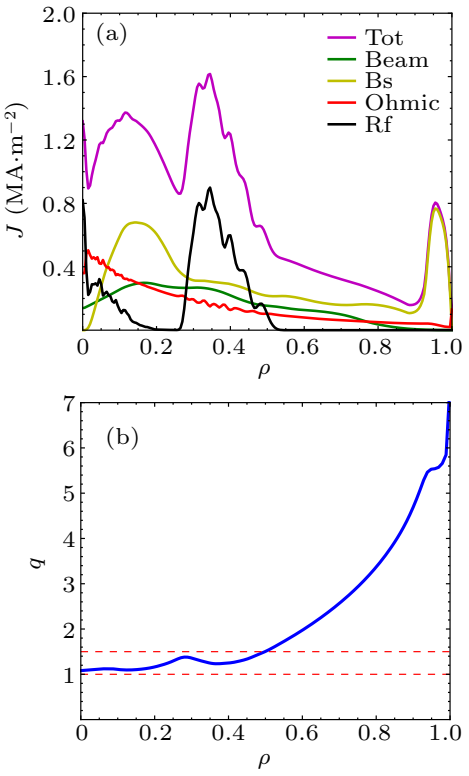


Fig. 4. (a) Current density profiles, with 'Tot', 'Beam', 'Bs', and 'Rf' representing total plasma current, current drive by neutral beam, bootstrap current, and the current drive by electron cyclotron wave, respectively; (b) q profile, in HL-3 hybrid scenario with high toroidal rotation.

To investigate the effect of toroidal rotation on the hybrid scenario, a new scenario with reduced torque is designed by applying 2.25-MW co-NBI and 2.25-MW counter-NBI. We can see from Fig. 5(a), that there is a decrease in beam-driven current, which is attributed to the counter-NBI. Fortunately, the enhanced Ohmic current compensates for this reduction, reinstating a flat q profile in the core. Besides, the position and power of ECW deposition remain the same as the scenario with high-torque, with the q profile in Fig. 5(b) showing minimal variance from Fig. 4(b). In our simulations, the ratio of fast ions generated by the co-NBI to fast ions generated by counter-NBI is kept equal to ensure consistent modeling of NB H & CD.

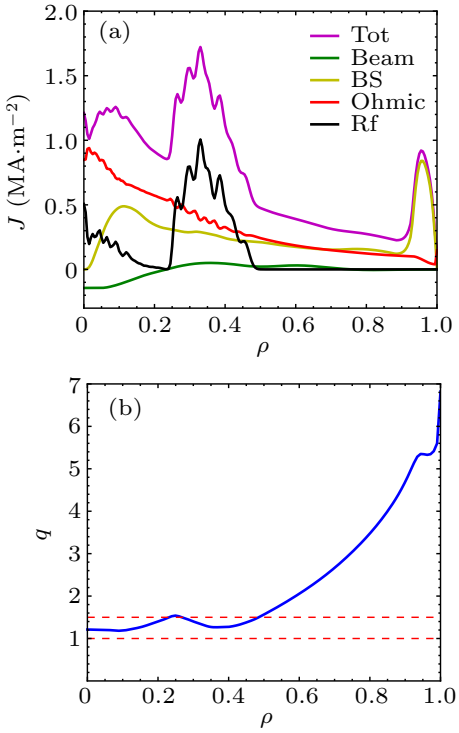


Fig. 5. (a) Current density profiles and (b) q profiles in HL-3 hybrid scenario with low toroidal rotation.

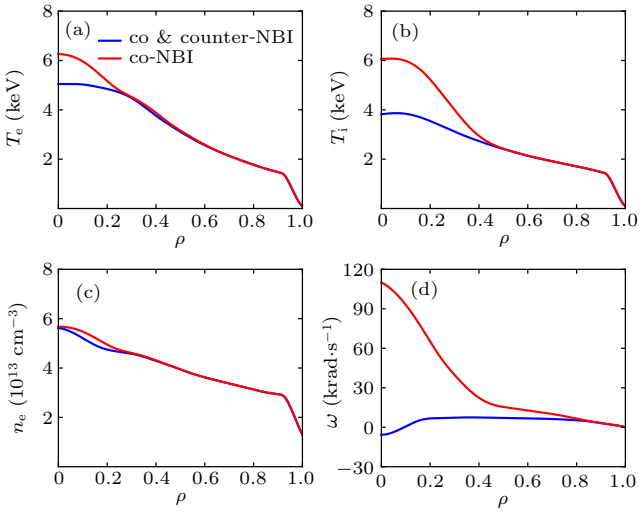


Fig. 6. Profiles of (a) electron temperature, (b) ion temperature, (c) electron density, (d) toroidal rotation velocity for two hybrid operation scenarios with the co-NBI (red line) and co- and counter-NBI (blue line).

The profiles of the two hybrid scenarios are compared in Fig. 6. Both scenarios exhibit a line averaged density close to 4.12×10^{19} m^{-3}, which is approximately half the Greenwald density limit (0.47 $f_{\rm G}$).[26] The core temperature of ion and electron are both lower in the low torque scenario than in the high torque scenario. With the application of the counter-NBI, the velocity of plasma decreases significantly from 1.1×10^5 rad/s to -5.6×10^3 rad/s.

The parameters for these two hybrid scenarios are listed in Table 4. From the table, it is obvious that even if the toroidal rotation velocity and the ion temperature decrease significantly, there is only a modest drop (10%) in stored energy.

Considering the distinct profiles observed in the two scenarios with different toroidal rotation velocities mentioned above, a detailed scan of the toroidal rotation is conducted, with the total heating power maintaining constant during the transition from high to low rotation. By adjusting the power ratios of co-NBI to counter-NBI, with other parameters fixed, five scenarios are compared, as shown in Table 5.

The results from various operation scenarios are illustrated in Fig. 7. Despite the rotation velocity changing, the temperature and density of the electrons remain similar. However, the ion temperature in the core region is significantly influenced by the rotation, experiencing a decrease from 6.07 keV to 3.97 keV. Notably, the ion temperature gradient follows a similar trend: decreasing with the rotation velocity declining at $\rho\sim0.4$. The decrease in ion temperature results in a decline in global confinement, as $H_{98,y2}$ decreases from 1.24 to 1.14.

Table 4. Main parameters of two hybrid operation scenarios with high and low toroidal rotation velocity.

Parameter	High toroidal rotation	Low toroidal rotation
W_0 (rad/s)	1.1×10^5	-5.6×10^3
$f_{\rm bs}$ (%)	49	43
$f_{\rm ni}$ (%)	86.9	64.7
$\beta_{\rm p}$	1.44	1.32
$\beta_{\rm N}/l_{\rm i}$	2.75/0.96	2.53/0.86
W (MJ)	0.80	0.73
W_ion (MJ)	0.33	0.28
W_electron (MJ)	0.47	0.45
$H_{98,y2}$	1.24	1.16

Table 5. Parameters for hybrid operations with different toroidal rotation velocities in HL-3.

Parameter	Case 1	Case 2	Case 3	Case 4	Case 5
Co-NBI (MW)	4.5	0.39375	3.375	2.8125	2.25
Counter-NBI (MW)	0	0.5625	1.125	1.6875	2.25
ECW (MW)	4.4	4.4	4.4	4.4	4.4
W_0 (rad/s)	1.1×10^5	6.9×10^4	5.5×10^4	2.3×10^4	-9.2×10^3
$n_{\rm e}$ (10^{19} m^{-3})	5.68	5.82	5.87	5.48	5.53
$T_{\rm e}$ (keV)	6.26	6.49	6.47	6.15	5.84
$T_{\rm i}$ (keV)	6.07	5.35	5.02	4.42	3.97
$f_{\rm bs}$ (%)	49	45	44	40.7	40.0
$f_{\rm ni}$ (%)	68	77	72	64.1	59.4
$\beta_{\rm p}$	1.44	1.40	1.38	1.33	1.31
$\beta_{\rm N}/l_{\rm i}$	2.75/0.96	2.67/0.97	2.66/0.93	2.56/0.92	2.51/0.93
W (MJ)	0.80	0.77	0.76	0.73	0.72
W_ion (MJ)	0.33	0.31	0.30	0.28	0.27
W_electron (MJ)	0.47	0.47	0.46	0.45	0.44
$H_{98,y2}$	1.24	1.20	1.19	1.16	1.14

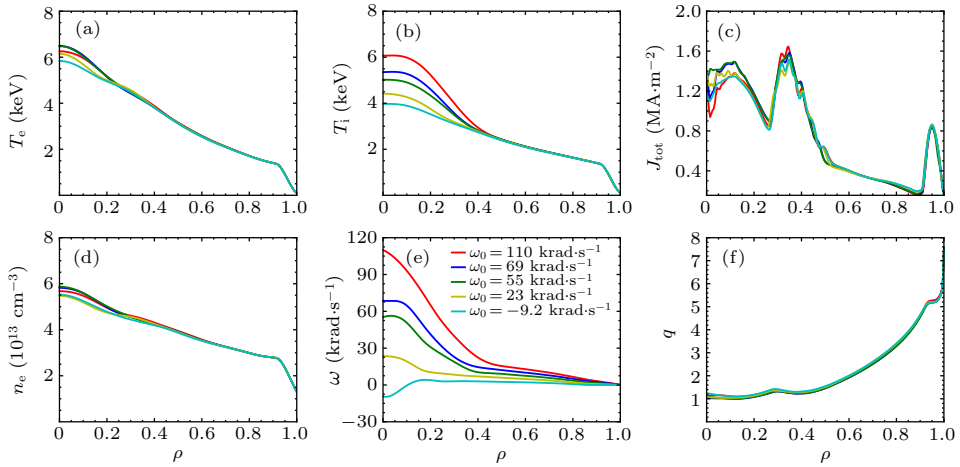


Fig. 7. Profiles of (a) electron temperature, (b) ion temperature, (c) current density, (d) electron density, (e) toroidal rotation, and (f) safety factor q of hybrid scenarios with different toroidal rotation velocities.

Figure 8 presents a comparison of the absorption power of ions and the transport coefficients between case 1 and case 5 from Table 5. Case 1 corresponds to the scenario with higher rotation velocity, while case 5 corresponds to the scenario with lower rotation velocity. The total power values obtained by the ion in the two cases are similar: both are about 3 MW. The turbulent transport coefficients of ion are 1.41 m^2/s and 0.63 m^2/s at $\rho = 0.38$ for case 5 (with lower rotation velocity) and case 1 (with higher rotation velocity), respectively. However, the neoclassical transport coefficients are almost the same in the core. This indicates that the differences among the ion temperature profiles are attributed to turbulent transport in the core plasma.

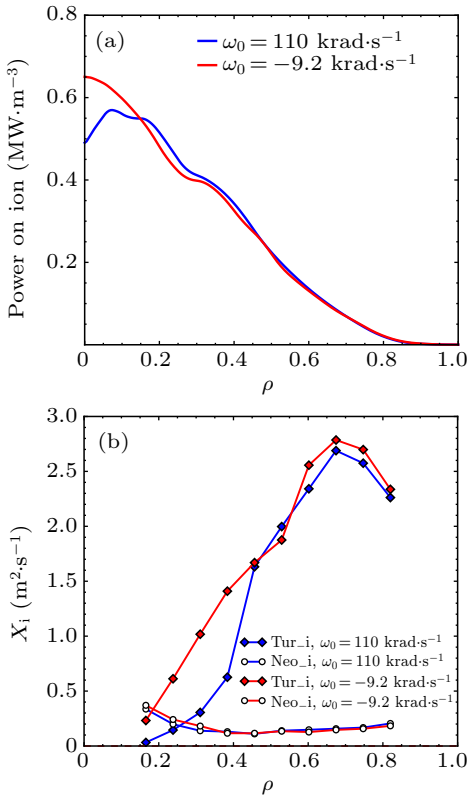


Fig. 8. (a) Total energy values absorbed by ions with different rotation velocities; (b) heat transport coefficients of ions with different toroidal rotation velocities.

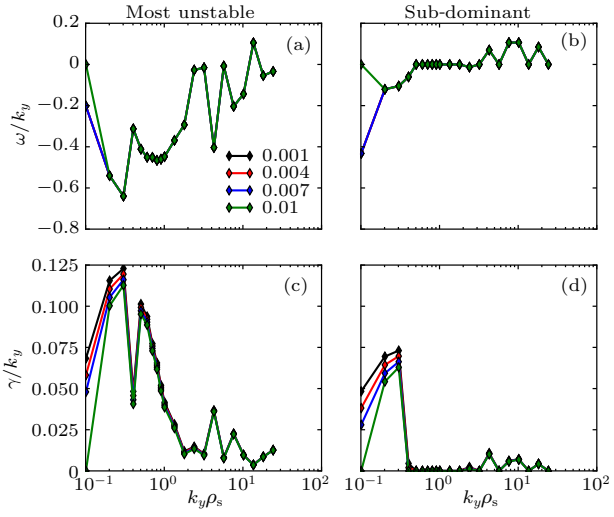


Fig. 9. Results of TGLF by scanning $E \times B$ shear, showing [(a), (c)] frequencies and [(b), (d)] growth rates of the most unstable mode and sub-dominant mode.

Since the $E \times B$ shear flow is closely related to toroidal rotation velocity, the $E \times B$ shear is scanned by the TGLF code. Here, the value of $E \times B$ shear is modified by scanning toroidal rotation. Figure 9 shows the frequencies and growth rates of the most unstable mode and sub-dominant mode at $\rho = 0.38$. It is observed that the modes with maximum growth rate correspond to poloidal wave numbers around $k_y\rho_s \sim 0.3$ and a frequency $\omega < 0$, indicating that the turbulence is dominated by ion temperature gradient (ITG) mode. Increasing $E \times B$ shear can suppress the ITG mode, thus reducing the transport level.

4. Effect of rotation on the hybrid scenario with high-density

In the HL-3 hybrid scenario with high rotation velocity, as discussed in Section 3, we scan the plasma densities by varying the pedestal top density (n_{ped}) in a range from 1.6×10^{19} m^{-3} to 5.6×10^{19} m^{-3}. The density profiles modeled by OMFIT are shown in Fig. 10(c). The reference case represented by the blue curve exhibits the value of n_{ped} of 2.6×10^{19} m^{-3}. It is worth noticing that the electron density profiles in $\rho < 0.8$ demonstrate significant stiffness, increasing almost linearly with the n_{ped}. During the simulation, the core q profiles of these scenarios are kept similar by adjusting the ECW. The NBI parameters are fixed as listed in Table 3, with the total power being co-injected. The rotation increases with density increasing until the n_{ped} reaches 4.7×10^{19} m^{-3}. Figure 11 shows the torques from NBI for the five scenarios. As the n_{ped} varies from 1.7×10^{19} m^{-3} to 5.7×10^{19} m^{-3}, the corresponding total torques generated by NBI are calculated to be 3.31 N·m, 3.63 N·m, 3.75 N·m, 3.79 N·m, and 3.78 N·m, respectively. It indicates that NBI provides an optimized high torque density.

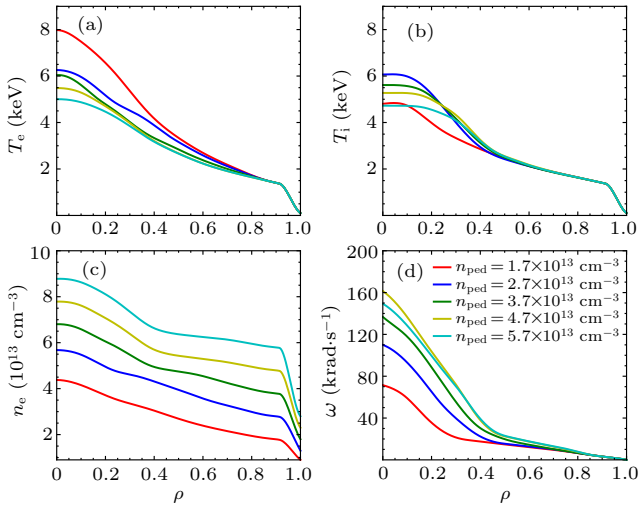


Fig. 10. Profiles of (a) electron temperature, (b) ion temperature, (c) electron density, and (d) toroidal rotation, for different values of n_{ped}.

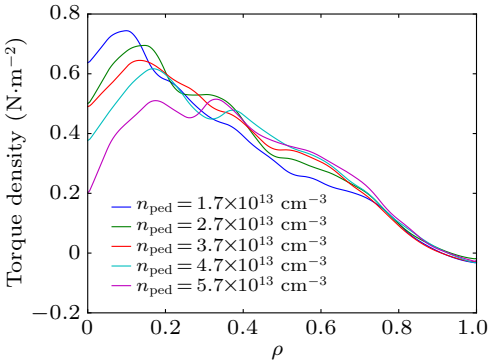


Fig. 11. Torque profiles for different densities.

To investigate the effect of rotation on the ion heat transport with different densities, the ion heat transport flux in the core is analyzed. Figure 12 shows a comparison of the neoclassical and turbulent transport fluxes among the aforementioned scenarios with different densities. As density ρ increases from 0.25 to 0.4, the collision is enhanced, resulting in the increase of neoclassical heat transport. Meanwhile, the ion turbulent heat flux decreases. It is notable that at higher density, particularly in the two cases with the n_{ped} values of 4.7×10^{19} m^{-3} and 5.7×10^{19} m^{-3}, the turbulent fluxes of ions are observed to be lower than neoclassical transport flux of ions in $\rho = 0.25$–0.4.

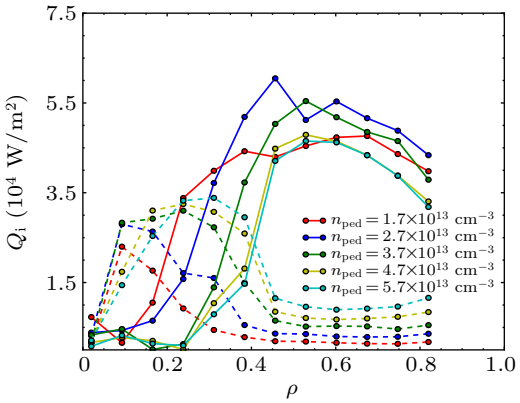


Fig. 12. Diagram of ion heat transport for different densities. From case 1 to case 5, the corresponding density ranges from low to high. The solid and dashed lines indicate turbulent and neoclassical transport fluxes, respectively.

For the high-density case ($n_{bar} \sim 7\times10^{19}$ m^{-3}, $n_{ped} \sim 5.7\times10^{19}$ m^{-3}), the NBI is divided into co-NBI injection and counter-NBI injection, each with beam power of 2.25 MW. The corresponding toroidal rotation angular velocity is 10^3 rad/s, as illustrated in Fig. 13(b). The difference in turbulent transport coefficient between the low rotation scenarion and high rotation scenario, $\Delta\chi_i$ is 0.04 m^2/s at $\rho = 0.38$ as shown in Fig. 13(d). For the lower density case with $n_{bar} \sim 4\times10^{19}$ m^{-3} (discussed in Section 3), the $\Delta\chi_i$ reaches a value as high as about 0.78 m^2/s. Furthermore, at high density ($n_{bar} \sim 7\times10^{19}$ m^{-3}), when the rotation velocity decreases to the order of 10^3 rad/s, the change in ion temperature is only $\Delta T_i \sim 0.3$ keV in the core (as shown in Fig. 13(c)). This suggests that the toroidal rotation velocity only slightly affects the ion confinement of high-density hybrid operation.

The comparison between Figs. 13(d) and 13(h) shows that the turbulent transport coefficient decreases greatly with density increasing in the ρ range of 0.2×0.4. In the core region, e.g., at $\rho = 0.38$, the ITG is dominant for the low-density case, but the electron temperature gradient (ETG) mode is dominant for the high-density case. Since the ETG mode is insensitive to the $E\times B$ shear,[27] the variation of transport coefficients could be neglected for the high-density case (Fig. 13(d)).

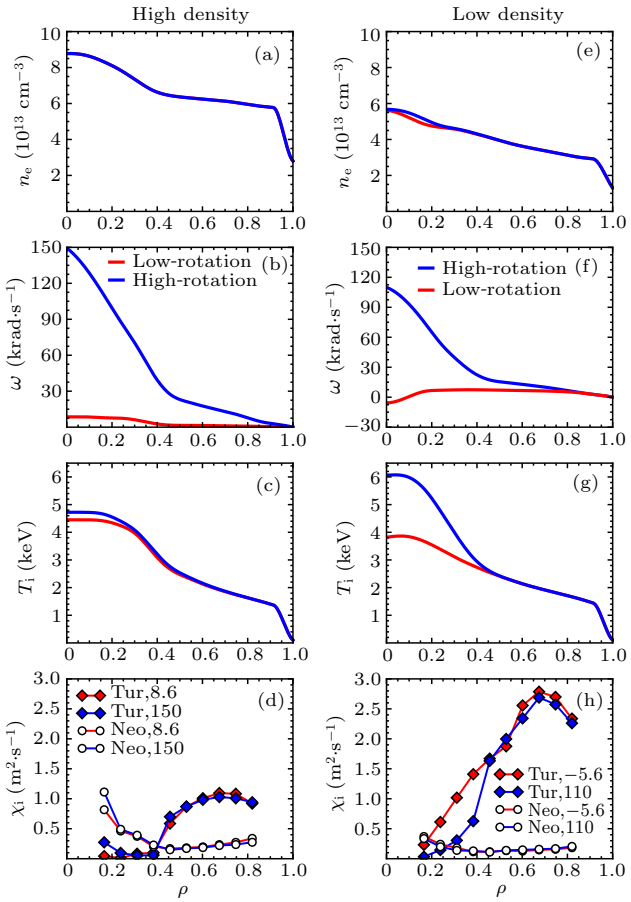


Fig. 13. Profiles of (a) electron density, (b) toroidal rotation, (c) ion temperature, and (d) transport coefficient in high-density scenarios, and profiles of (e) electron density, (f) toroidal rotation, (g) ion temperature, and (h) transport coefficient in low-density scenarios, with units in inset of panels (d) and (h) being all 1×10^3 rad/s.

5. Conclusions

This study investigated how toroidal plasma rotation affects the confinement of hybrid scenarios at various densities in the HL-3 by employing the OMFIT integrated modeling framework. At low density ($n_{bar} \sim 4\times10^{19}$ m^{-3}), the hybrid scenario is performed at $I_p = 1$ MA, $B_t = 1.9$ T, $P_{co-NBI} = 4.5$ MW, and $P_{ECW} = 4.4$ MW. The value of β_N and $H_{98,y2}$ can reach 2.8 and 1.24, respectively, and the corresponding toroidal rotation is 1.1×10^5 rad/s. Another scenario with co- and counter-NBI is modeled, in which rotation velocity is -5.6×10^3 rad/s. The decrease in rotation velocity leads the stored energy to drop from 0.80 MJ to 0.72 MJ. The core

ion temperature decreases from 6.1 keV to 3.8 keV, and the gradient of ion temperature becomes smaller. However, the rotation has little effect on the electron temperature and density. At $\rho \sim 0.38$, the turbulent heat transport coefficient of the ion increases from 0.63 m^2/s to 1.41 m^2/s.

However, the effect of rotation on the ion heat transport tends to be weak at high density ($n_{\rm bar} \sim 7 \times 10^{19}$ m^{-3}). At $\rho \sim 0.38$, the turbulent heat transport coefficients of the ion increase from 0.06 m^2/s to 0.10 m^2/s when the rotation velocity decreases from 10^5 rad/s to 10^3 rad/s. Consequently, this cause the ion temperature to drop slightly from 4.7 keV to 4.4 keV. It should be emphasized that the effect of rotation becomes relatively insignificant with higher densities. The neoclassical transport becomes stronger with high density, and the turbulent transport does not dominate the transport in the core anymore. Whilst, the rotation has almost no influence on the neoclassical transport in the core. These studies can provide support for the HL-3 hybrid scenario experiment in the next step.

Acknowledgements

We would like to express gratitude to the Supercomputing Center in SWIP for providing the computational resources for this research, and also to the General Atomic Theory Group for allowing the use of the OMFIT framework and GA codeset.

Project supported by the National Magnetic Confinement Fusion Program of China (Grants Nos. 2019YFE03040002 and 2018YFE0301101) and the Talent Project of China National Nuclear Corporation, China (Grant No. 2022JZYF-01).

References

[1] Shimada M, Campbell D J, Mukhovatov V, *et al.* 2007 *Nucl. Fusion* **47** S1

[2] Oyama N, Isayama A, Matsunaga G, Suzuki T, Takenaga H, Sakamoto Y, Nakano T, Kamada Y, Ide S and the JT-60 Team 2009 *Nucl. Fusion* **49** 065026

[3] Turco F, Petty C C, Luce T C, Carlstrom T N, Van Zeeland M A, Heidbrink W, Carpanese F, Solomon W, Holcomb C T and Ferron J R 2015 *Phys. Plasma* **22** 056113

[4] Hobirk J, Imbeaux F, Crisanti F, *et al.* 2012 *Plasma Phys. Control. Fusion* **54** 095001

[5] Igochine V, Piovesan P, Classen I G J, *et al.* 2017 *Nucl. Fusion* **57** 116027

[6] Staebler A, Sips A C C, Brambilla M, Bilato R, Dux R, Gruber O, Hobirk J, Horton L D, Maggi C F, Manini A, Maraschek M, Mück A, Na Y S, Neu R, Tardini G, Wade M R and ASDEX Upgrade Team 2005 *Nucl. Fusion* **45** 617

[7] Gormezano C, Sips A C C, Luce T C, *et al.* 2007 *Nucl. Fusion* **47** S285

[8] Jian X, Chan V S, Chen J L, Bock A, Zohm H, Fable E, Reisner M, Guo W F and Zhuang G 2019 *Nucl. Fusion* **59** 106038

[9] Burrell K H 1996 *Phys. Plasma* **4** 92186

[10] Garofalo A M, Ding S, Solomon W M, Grierson B A, Jian X, Osborne T H, Holland C, Knolker M, Laggner F M, Chrystal C, Marinoni A and Petty C C 2022 *Nucl. Fusion* **62** 056008

[11] Qian J P, Garofalo A M, Gong X Z, Ren Q L, Ding S Y, Solomon W M, Xu G S, Grierson B A, Guo W F, Holcomb C T, McClenaghan J, McKee G R, Pan C K, Huang J, Staebler G M and Wan B N 2017 *Nucl. Fusion* **57** 056008

[12] Petty C C, Kinsey J E, Holcomb C T, DeBoo J C, Doyle E J, Ferron J R, Garofalo A M, Hyatt A W, Jackson G L, Luce T C, Murakami M, Politzer P A and Reimerdes 2016 *Nucl. Fusion* **56** 016016

[13] Murakami M, Park J M, Giruzzi G, *et al.* 2011 *Nucl. Fusion* **51** 103006

[14] Duan X R, Xu M, Zhong W L, *et al.* 2023 29*th IAEA Fusion Energy Conference* (FEC 2023), 2023 October 16–21

[15] Meneghini O, Snyder P B, Smith S P, Candy J, Staebler G M, Belli E A, Lao L L, Park J M, Green D L, Elwasif W, Grierson B A and Holland C 2016 *Phys. Plasma* **23** 042507

[16] Meneghini O, Smith S P, Lao L L, *et al.* 2015 *Nucl. Fusion* **55** 083008

[17] Lao L L, Stjohn H, Stambaugh R D, Kellman A G and Pfeiffer W 1985 *Nucl. Fusion* **25** 1611

[18] Pfeiffer W W, Davidson R H, Miller R L and Waltz R E 1980 *ONETWO: a computer code for modeling plasa transport in tokamaks* p. 201

[19] Candy J, Holland C, Waltz R E, Fahe M R and Belli 2009 *Phys. Plasma* **16** 060704

[20] Snyder P B, Groebner R J, Hughes J W, Osborne T H, Beurskens M, Leonard A W, Wilson H R and Xu X Q 2011 *Nucl. Fusion* **51** 103016

[21] Goldston R J, McCune D, Towner H, Davis S, Hawryluk R and Schmidt G 1981 *J. Comput. Phys.* **43** 61

[22] Lin Y L, Chan V and Prate R 2003 *Phys. Plasma* **10** 4064

[23] Meneghini O, Snyder P B, Smith S P, Candy J, Staebler G M, Belli E A, Lao L L, Park J M, Green D L, Elwasif W, Grierson B A and Holland C 2016 *Phys. Plasma* **23** 042507

[24] Jian X, Chen J L, Chan V S, Zhuang G, Li G Q, Zhao D, Shi N, Xu G L, Gary M. Staebler G M and Guo W F 2017 *Nucl. Fusion* **57** 046012

[25] Chen J L, Jian X, Chan V S, *et al.* 2017 *Plasma Phys. Control. Fusion* **59** 075005

[26] Zheng X W, Li J G, Hu J S, *et al.* 2016 *Plasma Phys. Control. Fusion* **58** 055013

[27] Li J Q and Kishimoto Y 2004 *Phys. Plasma* **11** 1493